Interaction of three-dimensional hydrodynamic and thermocapillary instabilities in film flows

Benoit Scheid
Department of Chemical Engineering, Université Libre de Bruxelles C.P. 165/67, Avenue F.D. Roosevelt 50 - 1050 Bruxelles – Belgium

Serafim Kalliadasis
Department of Chemical Engineering, Imperial College London, London SW7 2AZ – UK

Christian Ruyer-Quil
Laboratoire FAST – UMR CNRS 7608, Campus universitaire, 91405 Orsay – France

Pierre Colinet
Department of Chemical Engineering, Université Libre de Bruxelles C.P. 165/67, Avenue F.D. Roosevelt, 50 - 1050 Bruxelles – Belgium

(Dated: November 11, 2008)

We study three-dimensional wave patterns on the surface of a film flowing down a uniformly heated wall. Our starting point is a model of four evolution equations for the film thickness h, the interfacial temperature θ and the streamwise and spanwise flow rates, q and p, respectively, obtained by combining a gradient expansion with a weighted residual projection. This model is shown to be robust and accurate in describing the competition between hydrodynamic waves and thermocapillary Marangoni effects for a wide range of parameters. For small Reynolds numbers, *i.e.* in the 'drag-gravity regime', we observe regularly spaced rivulets aligned with the flow and preventing the development of hydrodynamic waves. The wavelength of the developed rivulet structures is found to closely match the one of the most amplified mode predicted by linear theory. For larger Reynolds numbers, *i.e.* in the 'drag-inertia regime', the situation is similar to the isothermal case and no rivulets are observed. Between these two regimes we observe a complex behavior for the hydrodynamic and thermocapillary modes with the presence of rivulets channeling quasi-two-dimensional waves of larger amplitude and phase speed than those observed in isothermal conditions, leading possibly to solitary-like waves. Two subregions are identified depending on the topology of the rivulet structures that can be either 'ridgelike' or 'groovelike'. A regime map is further proposed that highlights the influence of the Reynolds and the Marangoni numbers on the rivulet structures. Interestingly, this map is found to be related to the variations of amplitude and speed of the two-dimensional solitary-wave solutions of the model. Finally, the heat transfer enhancement due to the increase of interfacial area in the presence of rivulet structures is shown to be significant.

PACS numbers: 47.15.gm,47.55.dm,47.85.g

I. INTRODUCTION

Interfacial flows are part of the general class of nonlinear systems with dissipation and dispersion. A thin viscous film flow driven by gravity [frequently referred to as 'falling liquid film'], in particular, can be used as a prototype system for the study of the route toward spatio-temporal chaos, *i.e.* a well-organized cascade of bifurcations leading from the flat film (or 'laminar') state to a state of disorder or turbulence (see *e.g.* [1]). In addition to the purely theoretical interest, falling liquid films play a central role in the development of efficient means for interfacial heat and mass transfer in a wide variety of engineering and technological applications, such as evaporators, heat exchangers, absorbers, scrubbers, rectification columns, crystallizers and falling film reactors. This is mostly due to the large surface-to-volume ratio and to the small heat and mass transfer resistance of a thin liquid film at relatively small flow rates. This resistance is further decreased by the presence of (wave) patterns at the interface of the film which typically lead to a significant enhancement of heat and mass transfer. Not surprisingly, therefore, falling liquid films have been an active topic of fundamental and applied research for several decades.

Three-dimensional (3D) hydrodynamic waves in isothermal falling films have been investigated experimentally by various authors (see e.g. [2]). Experiments by Liu, Schneider & Gollub [3] and more recently by Park & Nosoko [4] have provided a clear picture of the phenomenology and intricate dynamics of interacting 3D waves in isothermal film flows, that includes synchronously deformed fronts, subharmonic patterns and horseshoe-like waves. From the theoretical point of view and with the exception of direct 3D numerical simulations, the modeling of falling films generally relies on the 'boundary-layer approximation' in which the pressure is eliminated by integrating across the film the cross-stream component of the momentum equation where the inertia effects are neglected. This in turn removes the cross-

stream direction thus reducing the dimensionality of the problem by one. Hence, in this approximation 3D (resp. 2D) flows are represented by 2D (resp. 1D) equations.
Following the pioneering theoretical development of the 'integral-boundary-layer approximation' by the Russian school for 2D flows [5, 6] and 3D ones [7], Ruyer-Quil & Manneville [8, 9] obtained a 1D integral-boundary-layer model based on a high-order weighted residuals approach, which unlike the previous models, accounts correctly for the onset of the hydrodynamic instability. Recently, their model was extended to 2D and was shown to be capable of describing many of the complex 3D wave patterns observed in experiments for the isothermal case [10].
For heated walls, it is worth mentioning the pioneering experiment by Ludviksson & Lightfoot [11] who set up a film on a vertical solid plate of high heat capacity and thermal conductivity and heated with a constant downward directed temperature gradient leading to a cold top and warm bottom. An excellent summary of their findings is given in [12]:

> This situation leads to the creation of a series of parallel *roll cells* (*i.e.* rivulets), driven by lateral surface tension gradients ... A simple perturbation analysis shows that perturbations of some widths grow faster than others, setting up sinusoidal modulation in the transverse direction corresponding to the fastest growing mode. Such regularity is, however, seldom observed in practice. More commonly one sees occasional thick rivulets surrounded by large thin regions. These thin regions, taking up most of the available surface, are both slowly moving and quickly saturated and are thus ineffective for mass transfer. Only the rivulets are effective, and their total surface area is very small.

Hence the idea to increase the density of rivulets in order to enhance the heat/mass transfer. By imposing localized heating on an inclined water film, Kabov and coworkers [13–16] succeeded to observe regularized rivulet structures for a wide range of Reynolds numbers. The aim of the present work is precisely to propose a theoretical framework for the study of such regularized rivulet structure that allows to investigate the possible enhancement of the heat transfer.
Worth mentioning is the work by [17], who have studied the Marangoni effect in a single heated/cooled rivulet of prescribed volume preliminary formed and aligned with the slope of an inclined substrate, and whose contact angle with the substrate is also prescribed. They have explored the modification of the internal flow and the shape of the rivulet due to the Marangoni effect. Nevertheless, in contrast to their work, the rivulet structure we study here occurs spontaneously due to transverse thermocapillary instability and neither the volume, nor the 'apparent contact angle' near rupture are prescribed but depend instead on the regime considered. Furthermore, we will include inertia (not considered in [17]) that allows for hydrodynamic waves.
The linear stability analysis by Ludviksson & Lightfoot [11] considered the free surface as adiabatic thus demonstrating the crucial role of the imposed streamwise temperature gradient in the instability mechanism. On the contrary, Goussis & Kelly [18] analyzed the case of an inclined plate maintained at constant temperature, and showed that only a non-adiabatic free surface in this case can lead to the long-wave thermocapillary instability and concomitant streamwise roll cells, *i.e.* rivulets, A sketch of rivulet structures is given in Fig. 1. The mechanism in

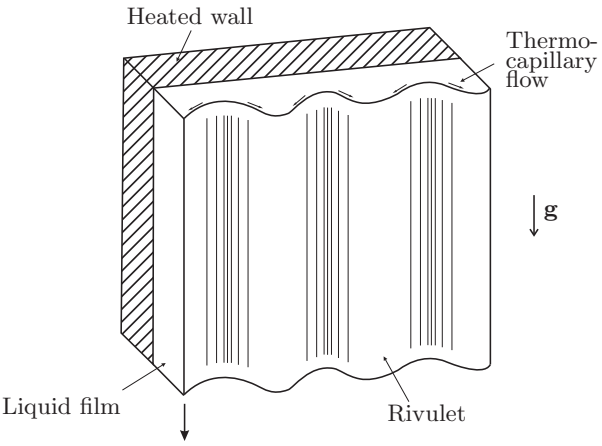

FIG. 1: Rivulet structure driven by thermocapillary effect at the surface of a falling liquid film heated from the wall.

this case is the same that the one described by Smith [19] to explain the dewetting of a thin film on a heated horizontal substrate: a spontaneous modulation of the free-surface elevation generates a temperature gradient at the interface and once flow starts, it is again maintained by the externally imposed temperature gradient (directed across the film). Goussis & Kelly [18] have therefore shown that a gravity-driven flow due to the plate inclination breaks the isotropy of the long-wave thermocapillary instability and aligns the structure with the flow. The wavelength of the instability, however, remains unchanged, at least in the linear regime.
Joo *et al.* [20] have modeled rivulet structure as predicted by [18] by using a nonlinear evolution equation for the film thickness based on the long-wave approximation, typically valid for small Reynolds numbers, up to $\mathrm{Re} = \mathrm{O}(1)$. However, their computer simulations experienced finite-time blow-up which is known to be unphysical and intrinsic to the Benney-type equation adopted by these authors [21]. Indeed, Ramaswamy *et al.* [22] have simulated the full Navier-Stokes and Fourier equations and they were able to follow the whole dynamics of rivulet formation, from onset up to rupture. Nevertheless, their computations were restricted to a small domain size and small Reynolds numbers. Ruyer-Quil *et al.* [23] have recently derived a 1D model that accurately describes the 2D wave dy-

namics of uniformly heated falling films up to moderate Reynolds numbers. In this study we extend the model developed in [23] to 2D. Our aim is to explore the 3D dynamics of a uniformly heated falling film in large-scale domains. We investigate in detail the influence of the Marangoni effect on the film dynamics up to moderate Reynolds number flows and the competition between the Marangoni effect and hydrodynamic waves, hence between rivulets/dry-spot formation and downward running surface waves. We also address the issue of heat transfer enhancement due to the presence of rivulets.

II. THE MODEL

Consider the flow of a Newtonian liquid falling down a uniformly heated vertical wall. A Cartesian coordinate system (x, y, z) is chosen so that x is the streamwise coordinate, y is the outward-pointing coordinate normal to the wall and z is the transverse coordinate. Our analysis is based on the boundary-layer approximation of the equations of motion and energy as well as associated wall and free-surface boundary conditions, which as was pointed out in § I removes the dependence on y so that the final equations depend on the in-plane coordinates x and z only.

The starting point of the boundary-layer approximation is to assume long-waves in both x and z directions, or equivalently, slow time and space modulations of the basic flat film solution (frequently referred to as the 'Nusselt flat-film thickness'), $\partial_t, \partial_x, \partial_z = O(\varepsilon) \ll 1$ with ε the 'film parameter' (unlike, however, the Benney long-wave approximation which typically leads to a single evolution equation for the film thickness for both isothermal and heated films, a direct consequence of slaving all variables to the kinematics of the interface, the boundary-layer approximation for heated films leads to a set of four coupled evolution equations as we shall demonstrate shortly). Subsequently, the pressure is eliminated from the momentum equation. As was pointed out in § I this step consists of integrating the y-component of the momentum equation across the film. By neglecting terms of $O(\varepsilon^3)$ and higher, the pressure takes the form (see [24] for details):

$$P = -(\partial_{xx}h + \partial_{zz}h) + \eta(\partial_y v + \partial_y v\big|_h) \,, \qquad (1)$$

where the first term on the right-hand side corresponds to surface tension and the second one to viscous stress. Substituting (1) into the x and z components of the momentum equation gives,

$$\delta\left[\partial_t u + \partial_x(u^2) + \partial_y(uv) + \partial_z(uw)\right] = 1 + \partial_{yy}u + \partial_{xxx}h + \partial_{xzz}h + \eta\left[2\partial_{xx}u + \partial_{zz}u + \partial_{xz}w - \partial_x(\partial_y v\big|_h)\right] , \quad (2a)$$

$$\delta\left[\partial_t w + \partial_x(uw) + \partial_y(vw) + \partial_z(w^2)\right] = \partial_{yy}w + \partial_{xxz}h + \partial_{zzz}h + \eta\left[2\partial_{zz}w + \partial_{xx}w + \partial_{xz}u - \partial_z(\partial_y v\big|_h)\right] , \quad (2b)$$

which together with the continuity equation,

$$\partial_x u + \partial_y v + \partial_z w = 0 \,, \qquad (2c)$$

constitute the *second-order boundary layer equations* [10] where h is the film thickness and u, v, w the streamwise, cross-stream and spanwise components of the velocity field, respectively. These equations together with the energy equation,

$$\mathrm{Pr}\delta\left[\partial_\mathrm{t} + \mathrm{u}\partial_\mathrm{x} + \mathrm{v}\partial_\mathrm{y} + \mathrm{w}\partial_\mathrm{z}\right]\mathrm{T} = \left[\partial_{yy} + \eta\partial_{xx} + \eta\partial_{zz}\right]T, \qquad (2d)$$

where T is the liquid temperature, are the dimensionless second-order boundary-layer equations in the presence of heat effects (the scaling is given below). $\mathrm{Pr} = \nu/\chi$ is the Prandtl number with ν the kinematic viscosity and χ the thermal diffusivity. The other dimensionless groups are the *rescaled Reynolds number* and *viscous dissipation number*, respectively,

$$\delta = \frac{(3\mathrm{Re})^{11/9}}{\Gamma^{1/3}} \qquad \text{and} \qquad \eta = \frac{(3\mathrm{Re})^{4/9}}{\Gamma^{2/3}} \,, \qquad (3)$$

which are based on the usual Reynolds and Kapitza numbers, respectively,

$$\mathrm{Re} = \frac{\mathrm{g}\bar{h}_\mathrm{N}^3}{3\nu^2} \qquad \text{and} \qquad \Gamma = \frac{\sigma}{\rho\nu^{4/3}\mathrm{g}^{1/3}} \,,$$

with g the gravitational acceleration, $\bar{h}_\mathrm{N}$ the thickness of the Nusselt flat-film solution, ρ the density and σ the surface tension. It should be emphasized that only the main contribution of the surface tension has been retained in the boundary-layer equations (2a-b) though it is formally of order ε^3. Higher-order curvature terms are consequently assumed to have negligible influence, something which has also been confirmed numerically. Therefore, in the asymptotic sense, $\Gamma = \mathrm{O}(\varepsilon^{-1/3})$ while $\mathrm{Re} = \mathrm{O}(1)$.

The parameters $\delta = O(\varepsilon)$ and $\eta = O(\varepsilon^2)$ result from the *Shkadov scaling* for isothermal films [6] and account for the separation of scales inherent to the boundary-layer theory. The lengthscales in the x and z directions are thus taken as $\kappa\,\bar{h}_\mathrm{N}$, $\bar{h}_\mathrm{N}$ is the lengthscale in the cross-stream y direction. Accordingly, the timescale is taken as $\nu\kappa/g\bar{h}_\mathrm{N}$ and the velocity scale as $g\bar{h}_\mathrm{N}^2/\nu$. The 'compression factor' $\kappa = 1/\sqrt{\eta}$ —inversely proportional to the film parameter ε—, is obtained by balancing the streamwise pressure gradient induced by surface tension $\propto \partial_{xxx}h$ with the streamwise gravity acceleration, equal to unity in (2a): $\kappa^{-1} = (\rho g\bar{h}_\mathrm{N}^2/\sigma)^{1/3}$. Notice that $\kappa \equiv \mathrm{We}^{1/3}$, with $\mathrm{We} = \sigma/(\rho\mathrm{gh}_\mathrm{N}^2)$ the Weber number. Finally, the temperature is taken relative to the temperature T_a of the far-field ambient gas and scales with $\Delta T = T_\mathrm{w} - T_\mathrm{a}$, with T_w the temperature of the wall (hence $T = 0$ corresponds to the ambient temperature T_a).

The set of momentum, energy and continuity equations (2) is closed by the no-slip/no-penetration boundary condition at the wall ($y = 0$), as well as the condition of constant temperature,

$$u = v = w = 0 \qquad \text{and} \qquad T = 1 \,. \qquad (4a)$$

At the free surface ($y = h$), the system is closed by the kinematic boundary condition, the projections of the tangential stress balance along the x and z directions, and the Newton's cooling law, respectively,

$$\begin{aligned}
\partial_t h &= -u\partial_x h - w\partial_z h + v\,, && \text{(4b)}\\
\partial_y u &= -\mathcal{M}\partial_x\theta + \eta\left[\partial_z h(\partial_z u + \partial_x w)\right.\\
&\quad \left. +2\partial_x h(2\partial_x u + \partial_z w) - \partial_x v\right]\,, && \text{(4c)}\\
\partial_y w &= -\mathcal{M}\partial_z\theta + \eta\left[\partial_x h(\partial_z u + \partial_x w)\right.\\
&\quad \left. +2\partial_z h(2\partial_z w + \partial_x u) - \partial_z v\right]\,, && \text{(4d)}\\
\partial_y T &= -\mathrm{B}\left(1 + \frac{1}{2}\eta\left[(\partial_{\mathrm{x}}\mathrm{h})^2 + (\partial_{\mathrm{z}}\mathrm{h})^2\right]\right)\mathrm{T}\\
&\quad +\eta\left[\partial_x h\partial_x T + \partial_z h\partial_z T\right]\,. && \text{(4e)}
\end{aligned}$$

The interfacial temperature $\theta = T\big|_{y=h}$ has been introduced using the relation

$$\left[(\partial_i + \partial_i h\partial_y)T\right]\big|_h \equiv \partial_i\theta \quad \text{with} \quad i = x, z.$$

Note that equations (4c–4d) have been truncated at $O(\varepsilon^2)$ and written in the frame of the 'one-sided approximation' [25], *i.e.* the dynamic viscosity, $\mu = \rho\nu$, of the surrounding gas is much smaller than that of the liquid so that the gas viscous stress at the free surface is negligible (e.g. $\mu_{\mathrm{air}}/\mu_{\mathrm{water}} = O(10^{-3})$). The first terms of the right-hand side of (4c–4d) correspond to the thermocapillary effect, i.e. tangential stress generated by surface tension gradient due to temperature gradient along the free surface. The dimensionless groups appearing in the free-surface boundary conditions are,

$$\mathcal{M} = \frac{\mathrm{Ma}}{\Gamma^{1/3}(3\mathrm{Re})^{4/9}} \qquad \text{and} \qquad \mathrm{B} = \mathrm{Bi}\,(3\mathrm{Re})^{1/3}\,, \quad (5)$$

which include the Marangoni and Biot numbers,

$$\mathrm{Ma} = \frac{\gamma\Delta\mathrm{T}}{\rho\nu^{4/3}\mathrm{g}^{1/3}} \qquad \text{and} \qquad \mathrm{Bi} = \frac{\alpha_{\mathrm{g}}\nu^{2/3}}{\mathrm{Kg}^{1/3}}\,,$$

with $\gamma = -\mathrm{d}\sigma/\mathrm{d}T$ the variation of surface tension with temperature, α_g the heat transfer coefficient that measures the rate of heat transport at the liquid-gas interface and K the thermal conductivity of the liquid.
The parameters $\{\delta, \eta, \mathcal{M}, \mathrm{B}\}$ are the Shkadov scaling for heated films. It is important to emphasize that besides revealing the intrinsic separation of scales in the boundary-layer approximation, another advantage of the Shkadov scaling is that all in-plane viscous dissipative and thermal diffusive terms —*i.e.* the terms of $O(\varepsilon^2)$ in the momentum/energy equations— are multiplied by the viscous dissipation number η. Hence, setting $\eta = 0$ straightforwardly reduces (2) to the *first-order boundary-layer equations* in the presence of heat effects. However, here, we shall proceed with second-order terms in η as our aim is the development of a model that accurately describes the 3D evolution of the film. And we know that in the isothermal case, second-order viscous dissipative effects have been shown to determine the amplitude and frequency of the capillary ripples in front of solitary humps [8, 9], that are in turn decisive in the wave pattern selection of 3D instabilities [10]. We thus expect that in the heated falling film the second-order viscous/thermal diffusive effects are also crucial for an accurate description of the free-surface/temperature waves. Further, the Shkadov scaling has the advantage that its parameters $\{\delta, \eta, \mathcal{M}, \mathrm{B}\}$ have values close to unity for common situations (e.g. $\delta \approx 1$ for water at 25°C, i.e. $\Gamma \approx 3000$, and for $\mathrm{Re} \approx 10$), which not only is convenient from the numerical point of view (in terms of convergence of the numerical scheme being employed) but also it makes the balance between all forces in the system (inertia, surface tension, viscosity, gravity and thermocapillarity) apparent.

Following the weighted residuals method together with a regularization procedure, as applied for the 2D heated case [23] and the 3D isothermal case [10], the three-dimensional system of equations (2) and boundary conditions (4) can be reduced to a two-dimensional model of four evolution equations for the thickness h, the streamwise and spanwise flow rates averaged across the film, q and p, respectively, and the interfacial temperature θ, all dependent only on time t and on the in-plane coordinates (x, z). This model, whose derivation details are given in appendix A, has the form:

$$\begin{aligned}
&\partial_t h = -\boldsymbol{\nabla}\cdot\mathbf{q}\,, && \text{(6a)}\\
&\delta\partial_t\mathbf{q} = \delta\left[\frac{9}{7}\left(\frac{\mathbf{q}\cdot\boldsymbol{\nabla}h}{h^2} - \frac{\mathbf{q}}{h}\cdot\boldsymbol{\nabla}\right)\mathbf{q} - \frac{8}{7}\frac{\boldsymbol{\nabla}\cdot\mathbf{q}}{h}\,\mathbf{q}\right]\\
&\quad +\bar{\bar{\mathcal{G}}}\left\{\frac{5}{6}h\,\mathbf{i} - \frac{5}{2}\frac{\mathbf{q}}{h^2} - \mathcal{M}\left(\frac{5}{4}\boldsymbol{\nabla}\theta - \frac{\delta}{224}hq\partial_{xx}\theta\,\mathbf{i}\right)\right.\\
&\quad +\frac{5}{6}h\boldsymbol{\nabla}\boldsymbol{\nabla}^2 h + \eta\left[\frac{7}{2}h\boldsymbol{\nabla}\cdot\left(\frac{\boldsymbol{\nabla}\mathbf{q}^T}{h}\right) + h\boldsymbol{\nabla}\cdot\left(\frac{\boldsymbol{\nabla}\mathbf{q}}{h}\right)\right.\\
&\quad +\frac{13}{4}\frac{\mathbf{q}\cdot\boldsymbol{\nabla}h}{h^2}\,\boldsymbol{\nabla}h + \frac{3}{4}\frac{\boldsymbol{\nabla}h\cdot\boldsymbol{\nabla}h}{h^2}\,\mathbf{q} - \frac{73}{16}\left(\frac{\mathbf{q}}{h}\cdot\boldsymbol{\nabla}\right)\boldsymbol{\nabla}h\\
&\quad \left.\left. -\frac{23}{16}\frac{\boldsymbol{\nabla}^2 h}{h}\,\mathbf{q} + \frac{13}{16}\left(\frac{\boldsymbol{\nabla}h}{h}\cdot\boldsymbol{\nabla}\mathbf{q} - \frac{\boldsymbol{\nabla}\cdot\mathbf{q}}{h}\,\boldsymbol{\nabla}h\right)\right]\right\}, && \text{(6b)}\\
&\delta\mathrm{Pr}\partial_{\mathrm{t}}\theta = 3\frac{(1-\theta-\mathrm{Bh}\theta)}{\mathrm{h}^2} + \delta\mathrm{Pr}\left[\frac{7}{40}(1-\theta)\frac{\boldsymbol{\nabla}\cdot\mathbf{q}}{\mathrm{h}}\right.\\
&\quad \left. -\frac{27}{20}\frac{\mathbf{q}\cdot\boldsymbol{\nabla}\theta}{h}\right] + \eta\left[\boldsymbol{\nabla}^2\theta + \frac{\boldsymbol{\nabla}h\cdot\boldsymbol{\nabla}\theta}{h} + (1-\theta)\frac{\boldsymbol{\nabla}^2 h}{h}\right.\\
&\quad \left. +\left(1-\theta-\frac{3}{2}\mathrm{Bh}\theta\right)\frac{\boldsymbol{\nabla}h\cdot\boldsymbol{\nabla}h}{h^2}\right], && \text{(6c)}
\end{aligned}$$

where $\boldsymbol{\nabla}=(\partial_x, \partial_z)$, $\mathbf{q}=(q, p)$, $\bar{\bar{\mathcal{G}}} = \{(\mathcal{G}_q, 0), (0, 1)\}$ and $\mathbf{i}$ is the unit vector in the streamwise direction. The regularization factor is $\mathcal{G}_q \equiv \left[1 - \frac{\delta}{70}q\partial_x h + \mathcal{M}\frac{5}{56}\frac{\partial_x\theta}{h}\right]^{-1}$. Equation (6a) is the mass conservation equation, (6b) is the in-plane momentum equation and (6c) is the energy equation. By construction, a gradient expansion of (6) leads exactly to the Benney equation written up to $O(\varepsilon^2)$, whose expression truncated at first-order for simplicity

yields the classical long-wave evolution equation [26],

$$\partial_t h + h^2\partial_x h + \frac{2}{15}\delta\,\partial_x(h^6\partial_x h) + \boldsymbol{\nabla}\cdot\left[\frac{h^3}{3}\boldsymbol{\nabla}\boldsymbol{\nabla}^2 h + \frac{h^2}{2}\frac{\mathcal{M}\mathrm{B}}{(1+\mathrm{B}h)^2}\boldsymbol{\nabla}h\right] = 0, \quad (7)$$

used frequently in thin-film studies [27]. On the other hand, in the absence of streamwise variation, i.e. $\partial_x = 0$, (6) truncated at first order ($\eta = 0$) as well as (7) both reduce to:

$$\partial_t h + \partial_z\left[\frac{h^3}{3}\partial_{zzz}h + \frac{h^2}{2}\frac{\mathcal{M}\mathrm{B}}{(1+\mathrm{B}h)^2}\partial_z h\right] = 0. \quad (8)$$

The model (6) is also fully consistent with the long-wave approximation of the Navier-Stokes and energy equations for $\varepsilon \ll 1$ and hence fully resolves the linear instability threshold whose cut-off wavenumbers in both directions read [18], respectively,

$$k_{\mathrm{c}}^{(x)} = \sqrt{\frac{2}{5}\delta + \frac{3}{2}\frac{\mathcal{M}\mathrm{B}}{(1+\mathrm{B})^2}}\,, \quad k_{\mathrm{c}}^{(z)} = \sqrt{\frac{3}{2}\frac{\mathcal{M}\mathrm{B}}{(1+\mathrm{B})^2}}\,. \quad (9)$$

And in this asymptotic limit, the wavenumber corresponding to the maximum growth rate is

$$k_{\max} = \frac{k_{\mathrm{c}}}{\sqrt{2}}\,. \quad (10)$$

Finally, note from (9) that the streamwise cut-off wavenumber is always larger than the spanwise one, due to the basic flow and the hydrodynamic instability. This also implies that the hydrodynamic mode always dominates the thermocapillary one in terms of growth rate, as first demonstrated in [18].

To summarize, the model (6) is asymptotically correct up to $O(\varepsilon^2)$. Moreover, it appears (a posteriori) to avoid unphysical divergences (finite-time blow-up) even outside the range of its strict asymptotic validity (see appendix A for details).

III. NUMERICAL RESULTS

A pseudo-spectral scheme with the spatial derivatives evaluated in Fourier space and the nonlinearities in real space has been employed to solve (6). The time dependence is accounted for by a fifth-order Runge-Kutta scheme which allows control of truncation errors by the difference with an embedded fourth-order scheme [28]. The time step is dynamically adapted to limit the relative error on each variable to $\leq 10^{-4}$. Aliasing has been treated by applying a low-pass filter whose cut-off frequency has been chosen in order to ensure the spatial convergence of the solution. It has been found that keeping only the first 2/3 of the Fourier modes in each direction and before each iteration was enough. The spatial convergence has been checked by doubling the mesh points in each direction with no qualitative difference in the patterns obtained, and more precisely by monitoring the energies of deformation E_x, E_z (see definitions below). Time-dependent simulations have been performed for both small and large domains. Notice that despite the apparent complexity of the system, all unknown variables are either averaged (flow rates) or interfacial quantities (film thickness/temperature) and hence the system in (6) is much more easily amenable to numerical analysis than full Navier-Stokes and energy equations. The computational domain of size $L_x \times L_z$ is discretized with $M \times N$ regularly spaced grid points with coordinates $x_i = iL_x/M$ and $z_j = jL_z/N$. The computations are terminated when the film thickness reaches a 'minimal thickness' of about $h \sim 10^{-3}$ for which long-range intermolecular forces cannot be neglected ($\sim$ 100nm). Consequently, we will refer to *rupture* when the film reaches this minimal thickness, independently of the subsequent dynamics that depends on the nature of these intermolecular forces (see *e.g.* [29, 30]), even though they could be easily incorporated in the model by a disjoining pressure term. Note, therefore, that the terms 'dewetting/rewetting' are used hereinafter to indicate the trend of the film thickness evolution in thin regions, i.e. locally decreasing/increasing, respectively.

We also define the energies of deformations in each direction as the quadratic sum of the Fourier coefficients obtained from the Fourier transform of each streamwise and spanwise profiles scanned over the whole computational domain [22]:

$$E_x(t) \equiv \frac{1}{MN}\sum_{j=1}^{N}\left(\sum_{m=1}^{M}|a_m(z_j,t)|^2\right)^{1/2}, \quad (11a)$$

$$E_z(t) \equiv \frac{1}{MN}\sum_{i=1}^{M}\left(\sum_{n=1}^{N}|b_n(x_i,t)|^2\right)^{1/2}, \quad (11b)$$

where the spatial Fourier coefficients are defined by

$$a_m(z,t) = \sum_{i=1}^{M} h(x_i,z,t)\,e^{\mathrm{i}\,2\pi m x_i/L_x}$$

$$b_n(x,t) = \sum_{j=1}^{N} h(x,z_j,t)\,e^{\mathrm{i}\,2\pi n z_j/L_z}\,,$$

and $\mathrm{i} = \sqrt{-1}$ is the imaginary unit. The relative values of these energies allow us to evaluate the three-dimensionality of the developed wave patterns and to quantify the direction of the deformation. As an example, $E_x \ll E_z$ indicates that the deformation occurs mainly in the transverse direction with practically no deformation in the streamwise direction (though we can still have flow in the streamwise direction).

As discussed in § II, one of the advantages of the Shkadov scaling is that its parameter values $\{\delta, \eta, \mathcal{M}, \mathrm{B}\}$ are close to unity. Nevertheless, several of the numerical results will be reported in terms of the usual parameters

$\{\mathrm{Re}, \Gamma, \mathrm{Ma}, \mathrm{Bi}\}$ which are more convenient for comparisons with experiments: indeed in this parametrization each of the physical quantities with which one might naturally control the experiment —such as the flow rate and the temperature difference $\Delta T = T_\mathrm{w} - T_\mathrm{a}$ or the heat transfer coefficient— appears in a single dimensionless group when the liquid-gas properties are fixed. On the other hand, for a given gas-liquid system and wall heating conditions, Γ, Ma and Bi are fixed and the only free parameter is the Reynolds number which is a flow-control parameter.

We finally note that the 3D model proposed does suffer from the same limitation with the 2D model developed by Scheid *et al.* [31] who reported non-physical negative temperatures (i.e., lower than T_a) for 2D solitary waves at sufficiently large Re. We have indeed observed negative temperatures in our computations in the region of large-amplitude/fast waves, e.g. for $\mathrm{Re} \gtrsim 10$. Such negative temperatures appear locally in space and in some occasions locally in time too. As a matter of fact, they seem to appear and disappear (again in the regime of high flow rates/large amplitude waves) but they do not seem to affect the main qualitative features of the dynamics. This deficiency of the 2D model has been prevented in a recent study by Trevelyan *et al.* [32] who showed that the previous 2D model gives qualitatively the same dynamics with the cured 2D one. We anticipate by analogy with the 2D case that the main results of the present study should be qualitatively similar to the extension of the study in [32] to the 3D case.

A. Small-size domain

We first validate our model by comparison with the small-size computations presented in the literature for small Reynolds number flows [20, 22], i.e. when a one-field model, such as that in (7) obtained by the Benney long-wave expansion, can still be valid ($\mathrm{Re} \sim 1$) ([20] utilized (7) and [22] full Navier-Stokes). The studies in [20, 22] provided evidence of rivulet formation based solely on thermocapillary instability phenomena. Figure 2 shows our simulation results corresponding to the simulations done in [22, Fig. 9] for $\mathrm{Re} = 1/3$, $\Gamma = 300$, $\mathrm{Ma} = 10$, $\mathrm{Bi} = 1$ and $\mathrm{Pr} = 7$. The computations are similarly performed with periodic boundary conditions (spectral method) and a simple harmonic disturbance of the form $h(x, z, 0) = 1 + 0.1\cos(k_x\, x) + 0.1\cos(k_z\, z)$ as initial condition. The wavenumbers k_x and k_z have been chosen with values below those for the maximum linear growth rate of instability modes in each direction, $k_{x\max} = 0.56$ and $k_{z\max} = 0.53$ —calculated from the long-wave limit (10) using (9), for the selected values of the dimensionless parameters — thus allowing for interesting secondary flow development (several modes may be unstable).

The initial perturbation corresponds to a trough in the center of the domain (a). Then, thermocapillarity sets in displacing the fluid from this hotter trough toward the surrounding colder crests. However, the growth rate of the hydrodynamic mode is dominant at the beginning and surface waves develop (b). As the local phase speed is proportional to the square of the local film thickness, the crests travel faster than the troughs leading to steepening of the wave as it grows (c). Due to the absence of mean flow in the spanwise direction, the liquid is more easily displaced laterally due to thermocapillarity. Hence, as time progresses the thinning of the liquid layer persists in the trough and forms a valley surrounded by rivulets aligned with the flow (d). This process is similar to the evolution of a heated thin film on a horizontal substrate [33]. Likewise, the inclined film exhibits the formation of a secondary rivulet between the main ones (e). As found by Boos & Thess [34], for horizontal layers a 'cascade of structures' takes place in thinner zones (f,g), prior to film rupture. The last stage prior to rupture obtained by Ramaswamy *et al.* [22, Fig. 9m] with direct numerical simulations (DNS) of the full Navier-Stokes and energy equations is at $t = 153$, in excellent agreement with (f), provided the time is multiplied by the scale factor $\kappa = 6.69433$ due to the different scaling employed here. Remarkably, our computation can continue beyond this time (up to $t = 175$) and reveals finer structures in the thin region and just prior to rupture (g). It is likely that the DNS performed in [22] was not capable of resolving the evolution of the passed $t = 153$ due to the choice of the number of mesh points in the normal direction. The authors would have most probably been able to compute the evolution for larger times with a refined grid resolution. However, this would have been at the expense of computational time, which demonstrates the significant advantage (especially for large Reynolds numbers and large system size) of working with a model of reduced dimensionality and in terms of interfacial/averaged variables such as the one proposed here.

Finally, figure 2(h) shows the energy of streamwise (spanwise) deformations E_x (E_z) given by (11). While E_z increases until the film ruptures, E_x increases first and then decreases continuously, showing that the presence of rivulets damps the evolution of hydrodynamic waves as time progresses and can eventually suppress them altogether: for small Reynolds numbers the system is thus dominated by the thermocapillary Marangoni effect.

Let us now increase only the flow rate, thus the Reynolds number to $\mathrm{Re} = 2$, while keeping the other physical parameters (Γ,Ma,Bi,Pr) the same. The rescaled Reynolds number becomes $\delta = 1.33$, which now lies outside the range of validity of the single evolution equation for the film thickness in (7), *i.e.* for $\delta > 1$ (the reader is referred to [21] for details). The streamwise and spanwise wavenumbers have been chosen to be $k_x \sim k_{x\max}/2$ and $k_z \sim k_{z\max}$, respectively, where the maximum linear growth rates occur for $k_{x\max} \approx 0.62$ and $k_{z\max} \approx 0.34$, as obtained from the long-wave limit (10) using (9). Figure 3 shows that the hydrodynamic mode quickly generates high amplitude waves (a,b) that lead to *solitary-*

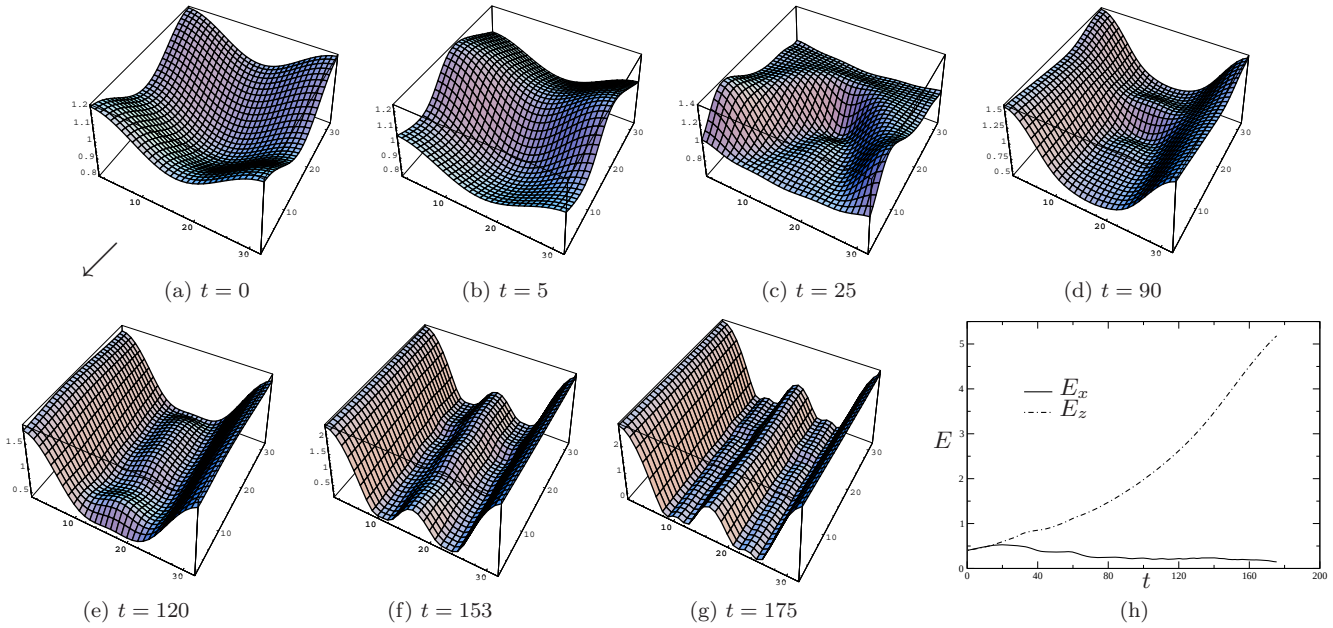

FIG. 2: Inception and development of rivulet aligned with the flow at different times computed with (6) for $\delta = 0.15$, $\eta = 0.022$, $\mathcal{M} = 1.5$, B = 1 and Pr = 7. The Reynolds number is Re = 1/3. The domain is a square with sides $2\pi/k_x$ with $k_x = k_z = 0.335$. The mesh consists of 32×32 points. The flow direction is indicated by the arrow. (h) Streamwise (E_x) and spanwise (E_z) energies of deformations (11) *versus* time.

like waves (c) —such waves are typically characterized by large amplitude and phase speed and their humps are preceded by capillary ripples. However, the thermocapillary mode causes film rupture before the surface wave fully develops. This is shown in Fig. 3*d* where both components of the energy of the streamwise and spanwise deformations E_x and E_z increase continuously in time but $E_x < E_z$ and the system is still dominated by the Marangoni effect. A remarkable interaction between the two instability modes is observed: as the thermocapillary flow feeds the core of the rivulet, the rivulet grows and the mean film thickness at the crest thus increases, along with the local flow rate. Hence, the wave profile at the crest of the rivulet does *not* saturate but rather follows the change of the 'local Reynolds number' by increasing its amplitude and its phase speed. This process terminates at $t > 620$ when the film is sufficiently close to the wall for the viscous stresses to slow down the lateral thermocapillary flow. The hydrodynamic wave and the longitudinal rivulet are found to coexist over a long time before the film ruptures.

B. Large-size domain

We now present large-size computations for a water film at 20°C ($\Gamma = 3375$, Pr = 7) with a temperature difference between the vertical wall and the ambient air of about 5°C (Ma = 50) and a large but realistic heat transfer coefficient of 1000W/m^{2}K at the liquid-gas interface, which yields Bi = 0.1. The time-dependent simulations are started with white noise of maximum amplitude 1/1000 of the flat film thickness $\bar{h}_{\rm N}$, which is itself varied between 32 and 146 μm (*i.e.* for $0.1 < {\rm Re} < 10$). The spatial mesh is fixed to 128×128.

Figure 4 shows again the formation of rivulets due to the Marangoni effect: the formation of circular patterns at early stages (a) reminiscent of the onset of (thermal) dewetting patterns on horizontal substrates [29, 30, 33, 35] (due to the small flow rate) is followed by the development of a 2D periodic wave train (b), a drop-like accumulation that breaks the 2D waves into 3D patterns (c,d) which then form meanders (e,f) prior to rivulet patterns aligned with the flow (g). As depicted previously in Fig. 3, the liquid then accumulates into rivulets, which increases the 'local Reynolds number' and fosters 2D solitary-like waves of larger amplitudes and phase speeds than those occurring for the same mean film thickness in isothermal conditions (h). This process

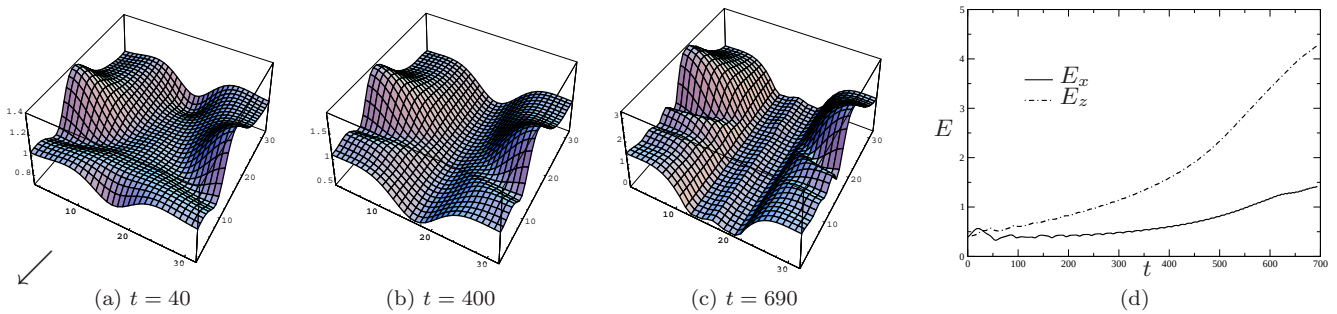

(a) $t = 40$ (b) $t = 400$ (c) $t = 690$ (d)

FIG. 3: Same as for Fig. 2 with for $\delta = 1.33$, $\eta = 0.05$, $\mathcal{M} = 0.674$, B = 1.82 and Pr = 7. The Reynolds number is Re = 2.

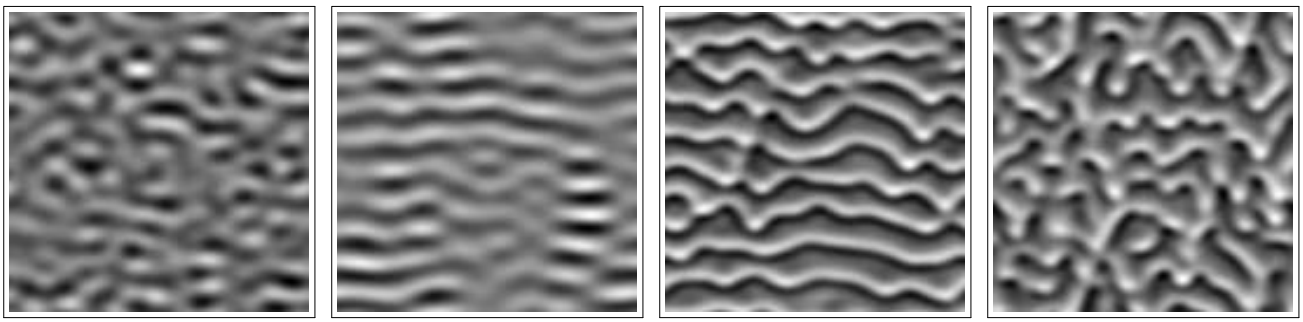

(a) $t = 100$ {0.998,1.002} (b) $t = 300$ {0.960,1.042} (c) $t = 500$ {0.825,1.210} (d) $t = 700$ {0.815,1.211}

(e) $t = 900$ {0.785,1.319} (f) $t = 1100$ {0.669,1.370} (g) $t = 1300$ {0.410,1.633} (h) $t = 1500$ {0.163,2.514}

FIG. 4: Water film free surface at different times calculated with (6) for $\delta = 0.6$, $\eta = 0.01$, $\mathcal{M} = 1.5$, B = 0.18 and Pr = 7. The periodic domain is a square of side $2\pi/k_x$ where $k_x = k_z = 0.05$. Bright (dark) zones correspond to elevations (depressions) of the film whose extrema are given in brackets.

continues until rupture of the film, a snapshot of which is shown in Fig. 5*a*.

Figure 5 shows that rivulet patterns still occur for Reynolds numbers up to Re = 5 (snapshot near rupture) whereas they do not appear for larger values. For Re = 6, the wave patterns on the interface are similar to those observed in isothermal conditions (see *e.g.* [2, 4, 10]) even though channels aligned with the flow can be observed in some places and seem to be the precursor to rivulet formation. In fact, rivulet structures never show up, for at least a long period of time —10000 time units, corresponding to several meters in a real experiment— dur-

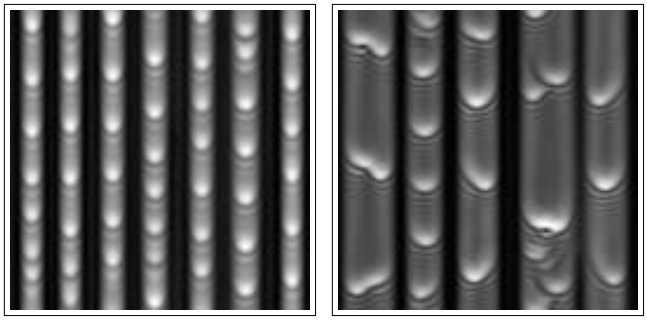

(a) $\delta = 0.6$, $t = 1800$ {0.018,3.010}

(b) $\delta = 1.83$, $t = 3520$ {0.004,3.410}

(c) $\delta = 2.28$, $t = 5720$ {0.675,1.961}

(d) $\delta = 4.26$, $t = 860$ {0.236,2.992}

FIG. 5: Wave patterns for various Reynolds numbers: (a) Re = 2, (b) Re = 5, (c) Re = 6 and (d) Re = 10 and with fixed $\Gamma = 3375$, Ma = 50, Bi = 0.1 and Pr = 7. Values for η, $\mathcal{M}$ and B used for computations can be recovered with the help of (3) and (5). The times for (a) and (b) are the times near rupture. Extrema of the film thickness are given in brackets.

ing which a 'stationary' wave regime takes place with a nearly constant energy of deformations in both directions: $E_x \approx E_z \approx cst$. The dynamics is characterized by a competition between the mean flow that continuously rewets the substrate and the Marangoni effect that tries to break the film. For Re = 6 the mean flow is strong enough so that the Marangoni effect cannot cause film rupture (clearly this depends on the Marangoni number, e.g. for Ma = 100, we would also have rivulets for Re > 6 as shown later). Notice, however, that solitary-like structures separated by relatively flat zones are not observed for Re = 6, instead they are present for Re = 10 as shown in Fig. 5*d*. Notice also that in these conditions, waves are typically characterized by large amplitudes and high phase speeds with their humps always preceded by capillary ripples.

IV. MAP OF REGIMES

As shown by Ooshida [36], for isothermal films 2D solitary waves (primary homoclinic orbits of the associated dynamical system) experience a 'steep' increase of both phase speed and amplitude as the Reynolds number increases, indicating the existence of two different regimes: (i) the *drag-gravity regime*, for small Re, where gravity is mainly balanced by the viscous drag with inertia playing only a 'perturbative' role which is balanced in turn by the surface tension; (ii) the *drag-inertia regime*, for larger Re, characterized by the dominant role played by inertia that interacts with the viscous drag to form a long tail to the back of the wave, which varies like δ [36]. With the aim to classify the different patterns observed depending on the Reynolds number, we have identified an interesting correlation between the behavior of the developed 3D wave patterns and such 2D solitary waves for non-isothermal conditions (such waves were constructed in [31]). This is illustrated in Fig. 6: for small Reynolds number flows where 2D solitary waves have small amplitudes and speed (region I), rivulet structures always occur and grow until spontaneous rupture. Here, the waves only slightly perturb the dry patch formation mechanism already known for horizontal films [35]. On the contrary, for large Reynolds number flows where 2D solitary waves have large amplitude and velocity (region III), no rivulet structures appear and the film behaves like in isothermal conditions. In terms of wave regimes, region I that corresponds to the drag-gravity regime in isothermal conditions, under heating is rapidly dominated by thermocapillary effects, whereas region III that corresponds to the drag-inertia regime in isothermal conditions is still dominated by inertia effects, which implies little or no influence of thermocapillarity. The transition between these two regions is located between the dot-dashed lines in Fig. 6 determined with an accuracy of ± 0.25 on the Reynolds number (region II). This region corresponds to the most interesting case of interaction between rivulet structures driven by the Marangoni effect and hydrodynamic waves. The boundaries between the different regions can also be characterized by the evolution in time of the energies of deformations near rupture, as follows: region I: $E_x \searrow$ and $E_z \nearrow$; region II: $E_x \nearrow$ and $E_z \nearrow$; region III: $E_x \approx E_z \to cst$ (no film rupture). Note that rivulet structures (regions I and II) are always characterized by $E_z > E_x$. As far as the hydrodynamic waves are concerned, we can additionally make the following classification, referring to Fig. 6:

- I the hydrodynamic waves are damped in time and the dynamics is dominated by rivulets until rupture (case of Fig. 2).
- $\mathrm{II_w}$ regular quasi-2D wave-trains are present at the crest of rivulets (case of Figs. 3 and 5*a*).
- $\mathrm{II_m}$ transversely modulated quasi-2D waves occur at the crest of rivulets (case of Fig. 5*b*).
- III patterns of fully developed 3D waves without film rupture (case of Fig. 5*c*-*d*).

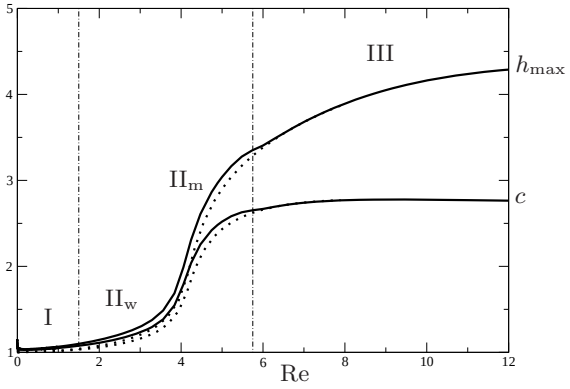

FIG. 6: Phase speed c and maximum film thickness $h_{\max}$ of 2D solitary-wave solutions (solitons) *versus* Re for Ma = 50 (solid line) and Ma = 0 (dotted line), for Bi = 0.1, Pr = 7 and $\Gamma = 3375$. The dot-dashed lines show the boundaries between the different regions.

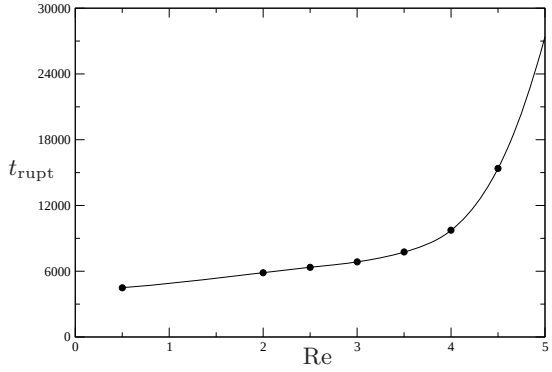

FIG. 7: Rupture time t_{rupt} estimated when $h = O(10^{-3})$ *versus* Re for Ma = 25, Bi = 0.1, Pr = 7 and $\Gamma = 3375$. Points from simulations are interpolated/extrapolated by the solid line.

V. MECHANISMS FOR REGIME TRANSITIONS

Mechanism for the transition I–II: In the 2D case, the Marangoni effect reinforces the hydrodynamic instability. This is illustrated by the speed and amplitude of the single-hump (2D) solitary waves that are larger at Ma = 50 than at Ma = 0 in Fig. 6 (this effect is discussed in detail in [31]). The same effect is also present in the 3D case: as already pointed out in § III, the rivulets accumulate fluid and thus help increasing the local substrate thickness, which again is in favor of the hydrodynamic instability (increasing local Reynolds number). Yet, the formation of rivulets has also a rather subtle stabilizing effect on the waves. As the width of the rivulets remains fixed independently of any changes in their amplitude due to the quasi-2D waves riding on them (this is evident from Fig. 8a to be discussed later), the spanwise curvature $\partial_{zz}h$ increases with the thickness h, and therefore the induced capillary pressure is larger in the humps than in the flat zones between the humps which then creates a pressure gradient that drags some liquid out of the humps and thus reduces their amplitudes (indeed Fig. 8b reveals that the wave amplitudes are not as large as they would have been based on the local Reynolds number, precisely due to the stabilization effect of the spanwise curvature). The competition between these two mechanisms is responsible for the transition I–II, i.e. when the increase of wave amplitudes due to the increase of the local Reynolds number wins over the stabilizing effect of the spanwise curvature following the shape of rivulets. It is important to emphasize here that the role of the spanwise curvature is different to that in other problems such as film flows down fibers [37, 38] where the spanwise curvature always has a destabilizing effect since it is smaller in the drops than on flat zones between the drops, thus promoting flow from the flat zones to the drops, leading to larger amplitudes (the mechanism for the drop formation process is nothing else but the classical Rayleigh instability of a liquid cylinder).

Mechanism for the transition II_w–II_m: Figure 5*b* shows that the quasi-2D solitary waves riding the rivulets experience a transverse instability, which, however, does not lead to the complete disintegration of the solitary waves. It is precisely for this reason that we have referred to the waves in Fig. 5*b* as 'quasi-2D solitary waves' much like those in Figure 5*a*. To explain this transition, an analogy can be made with 2D solitary waves on a vertical planar substrate. In this case isolated 2D solitary waves experience an instability in the transverse direction. This instability has a 3D origin unlike the case of small inclination angles where 3D instabilities have a 2D origin and are only observed for periodic 2D waves while isolated 2D solitary waves are stable [3]. The instability of 2D periodic waves was recently analyzed in detail by Scheid *et al.* [10]. On the other hand, the studies in [39, 40] on the transition of 2D pulses to 3D ones, revealed that the instability is strongly connected with the hump of a 2D pulse and in fact the main instability mechanism for the transition to 3D pulses is a Rayleigh-type instability of the solitary hump (see also section VII).

Mechanism for the transition II–III: This transition occurs at the Reynolds number above which the film does not rupture. This boundary is difficult to determine with sufficient accuracy and rather corresponds to a limit of infinite time required for the thermocapillary effect to cause film rupture. This is illustrated by the rapid increase of the rupture time with the Reynolds number in Fig. 7. In any case, one expects physically that there should exist a Reynolds number above which the flow is sufficiently strong to continuously rewet the thin parts of the film thus preventing rupture for all times.

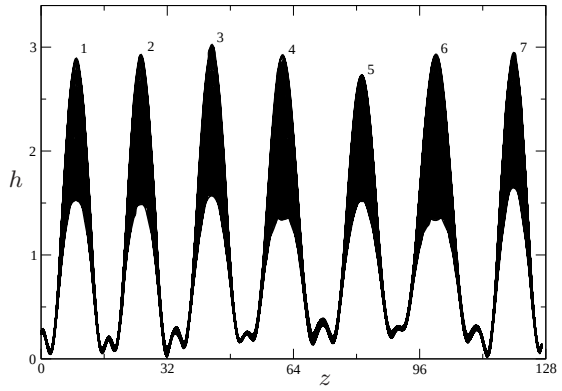

(a)spanwise profile of rivulets

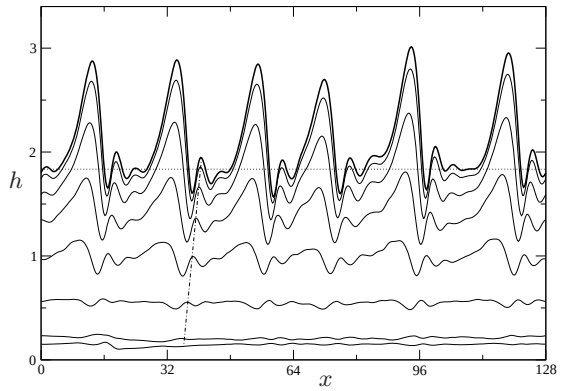

(b)streamwise profiles along the left side of rivulet 3

FIG. 8: Cross-sections of Fig. 5*a* for Re = 2: (a) 128 profiles are drawn, hence the dark area. (b) the dashed line shows the approximative local substrate thickness of the profile at the crest (thick solid line). The dot-dashed line is the locus of a local maximum, which shows the curvature of the wave front.

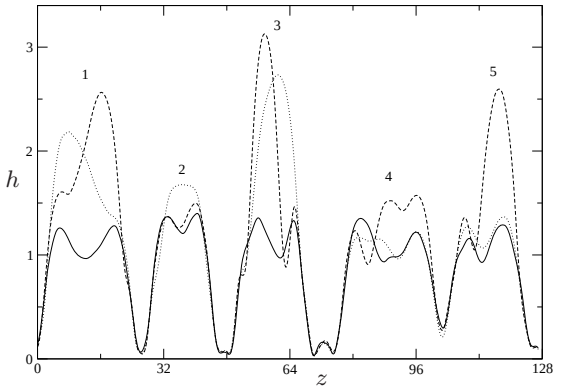

(a)spanwise profile of rivulets

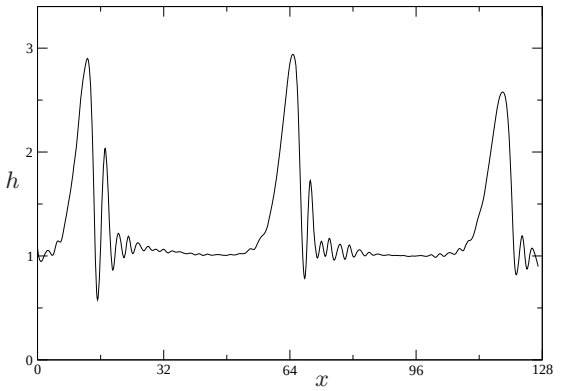

(b)streamwise profile of rivulet 1

FIG. 9: Cross-sections of Fig. 5*b* for Re = 5.

VI. TOPOLOGY OF RIVULET STRUCTURES

Figure 8 depicts typical cross-sections for the type $\mathrm{II_w}$. The spanwise cross-section (a) shows (in dark) the locus of the interface, thus revealing a *ridgelike structure*. The streamwise cross-section (b) shows eight profiles along the left side of rivulet 3 taken between the trough and the crest. Figure 8*a* shows that the maxima of rivulets vary by a factor of ~ 2 due to the presence of hydrodynamic waves riding them. However, the rather symmetric shape of their envelope indicates that their positions are stable and well aligned with the main flow. It also implies that rupture of the film occurs at two single spots (in fact between rivulets 2–3 and 6–7). Interestingly, rivulets 4 and 6 on Fig. 8*a* are wider than the others and the minimum of their crest is slightly upside-down, implying that their crest can have a local trough (this feature is however more pronounced in regime $\mathrm{II_m}$ as shown below). Fig. 8*b* reveals that the the rivulet crest (thick line) has waves of much larger amplitudes and phase speeds than predicted in the absence of rivulets (see Fig. 6). Taking arbitrarily the dotted line in Fig. 8*b* as the film substrate of the wave train at the crest, we can estimate the 'local Reynolds number' as $1.8^3 \sim 5.8 \times Re$. Consequently, the wave amplitude is much larger than it would have been without heating for Re = 2 but not as high as that corresponding precisely to the local Reynolds number ~ 11.6 due to the stabilizing effect of the spanwise curvature as was pointed out in § V,. Note also the wave front is curved backwards on the sides as also depicted by the oblique dot-dashed line in Fig. 8*b*, reminiscent of tails in 3D solitons [41].

Figure 9*a* shows cross-sections for the type $\mathrm{II_m}$ at three different streamwise positions. The rivulets here have sharp sides and wide tops displaying trough in the middle. They are strongly asymmetric, a signature of transverse instabilities. The valleys between neighboring rivulets are much more narrow than the rivulets themselves. Therefore the local Reynolds number at the top of the rivulets is closer to the inlet Reynolds number. Moreover, the presence of the rivulets promotes 2D waves instead of 3D ones. As a consequence, the wave amplitude gets closer to the one of the corresponding 2D solitary waves (see Fig. 6). The existence of such 2D solitary wave solutions is responsible for the presence of isolated solitary-like pulses as shown in Fig. 9*b*. We believe this

regime to be quite interesting for experimental investigations of quasi-2D solitary waves in the region of moderate Reynolds numbers since, although spanwise instabilities are not prevented all-together, the interface does not disintegrate into a fully developed 3D wave regime as it is the case with falling films on planar substrates, or in the present problem for *e.g.* Re = 6 where the surface of the film is covered by 3D waves with smaller amplitudes, without being separated by flat zones (see Fig. 5*c*) (recall that increasing the Reynolds number to *e.g.* Re = 10 causes the formation of isolated 3D solitary pulses (pulses separated by flat regions)). To our knowledge, the only other system where purely 2D solitary waves can be stabilized has been proposed in the experiments by Alekseenko *et al.* [42], which consist of a rivulet flowing beneath the outer surface of an inclined cylinder.

Further, we note that the last two rivulets in Fig. 5*b* (rivulets 4 and 5 in Fig. 9*a*) are separated by a relatively thick film region instead of the thin films separating the rest of the rivulets. The situation here looks more like 'grooves' that split the film into channels wide enough for the 3D hydrodynamic waves to survive. The transition then between types II_w and II_m corresponds to the transition between ridgelike structure and *groovelike structure*.

VII. WAVELENGTHS OF SPANWISE STRUCTURES

Figure 10 depicts the wavelength of the spanwise rivulet structures (ridgelike or groovelike) as obtained from time-dependent simulations (circles). The wavelength is obtained by dividing the width of the domain in the transverse dimension, L_z, by the number of rivulets. The results are similar to those obtained from the spanwise power spectrum. The error bars are due to a small variation of the number of rivulets for the same conditions due to the white noise initial condition changing each time the noise generator is ran (still, the maximum amplitude of the noise is always fixed at 1/1000). The solid line gives the wavelength of the most amplified mode found from the linear stability analysis of the full Navier-Stokes and energy equations obtained by suppressing the variation in the streamwise direction (the pure thermocapillary problem), which in dimensionless form yields:

$$\lambda_{\mathrm{riv}} \equiv \frac{2\pi}{k_{z\max}} = \frac{4\pi(1+B)}{\sqrt{3\mathcal{M}B}}\,, \qquad (12)$$

where (9) and (10) have been used. Utilizing now the definitions of dimensionless parameters given in section II and the length-scale $\kappa\bar{h}_{\mathrm{N}} = (\Gamma\nu^2/\mathrm{g})^{1/3}(3\mathrm{Re})^{1/9}$, the dimensional wavelength of the most amplified linear mode is $\propto \mathrm{Re}^{1/6}$ (solid line). It matches particularly well with our computations with Ma = 50 for small Reynolds numbers, *i.e.* in region I, but diverges for larger Reynolds numbers, *i.e.* in region II. This reveals the net influence of hydrodynamic waves and thus inertia effects on the wavelength of the rivulet structures. Nevertheless, the linear result seems a good estimate of the observed wavelength of the developed nonlinear rivulet structures and can therefore be used to examine the influence of a 'large' temperature difference across the layer, $\Delta T \approx 10°\mathrm{C}$, *i.e.* for Ma = 100. In this case we find a surprisingly good agreement between the linear theory which gives precisely $\lambda_{\mathrm{riv}}(\mathrm{mm}) = 7.52(1 + 0.144\mathrm{Re}^{1/3})\mathrm{Re}^{1/6}$ and the experimental fit given by Kabov *et al.* [13, 14], $\lambda_{\mathrm{riv}}(\mathrm{mm}) \approx 8.9\mathrm{Re}^{1/6}$. However, our numerical procedure has several differences with these experiments: (i) the wall temperature is not controlled in the experiment but rather the heat flux, hence the wall temperature varies along the flow direction and a precise value of the temperature difference ΔT needed for comparison is not available. (ii) our simulations do not include the lateral boundaries, nor the fact that the heater is finite *i.e.* embedded only in a portion of the wall and at a certain distance from the inlet. A bump at the upper edge of the heater therefore appears [43], which is known to significantly modify the wavelength of the rivulet structures [44, 45]. Moreover, periodic boundary conditions used here to minimize the computational domain and take advantage of the good convergence properties of the spectral method, are basically unrealistic. Indeed, closed flow configurations cannot be obtained experimentally; it therefore introduces an artifact: the fluid coming out from the outlet is re-introduced to the inlet. Besides some artificial finite size effects generated by the limited streamwise extension of the numerical domain – which have been essentially reduced by considering extended domains – periodic boundary conditions in our simulations rather correspond to an experiment where the entire wall is heated, *i.e.* from the inlet to far downstream (about a meter). Indeed, as the hydrodynamic instability has a convective nature, the position of the heater in existing experiments [13, 14] has a strong influence on

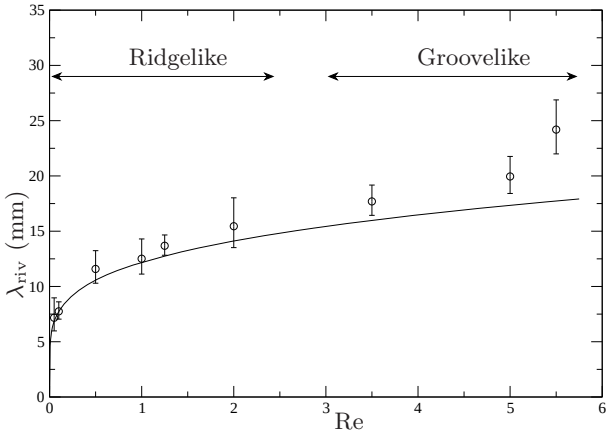

FIG. 10: Wavelength of the rivulet structures, $\lambda_{\mathrm{riv}}(\mathrm{mm})$, *versus* Reynolds number for the case of Fig. 5, obtained from large-size computations (circles). The solid line corresponds to the linear result (12).

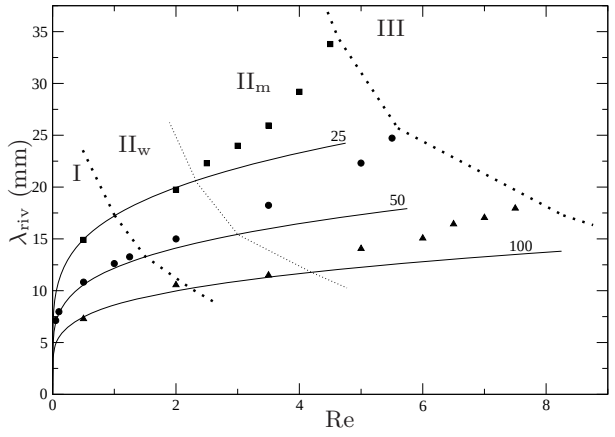

FIG. 11: Wavelength of the rivulet structures, $\lambda_{\rm riv}$, *versus* Reynolds number for Ma = 25 (square), Ma = 50 (circles) and Ma = 100 (triangle). The solid lines correspond to the linear prediction. The dotted lines indicate the approximate boundaries between the different regimes as referred to in Fig. 6.

the interaction of waves with the development of rivulet structures. As far as we are aware, such extended uniform heating has not been investigated experimentally as of yet and comparisons of our results with experiments on finite-size heaters should be done with caution.

VIII. INFLUENCE OF THE MARANGONI EFFECT

Figure 11 shows the influence of the Marangoni effect on the wavelength of rivulet structures: this is the full regime map in the Re $-$ λ space *versus* Ma. As before, the transition I-II is obtained when E_x changes from decreasing to increasing and the transition II-III is obtained when the dynamics of the film changes from one that eventually leads to rupture to one where rupture does not occur (right dotted line). Now, Fig. 11 offers the possibility to quantify also the transition II$_{\rm w}$-II$_{\rm m}$. Indeed, it appears to correspond to the departure of the wavelength from its linear prediction. Moreover, we have performed streamwise-independent simulations (not shown) and found that the resulting rivulets' wavelengths match well the linear curves for all Re: this indicate that second-order viscous dissipation does not play a significant role in the evolution of nonlinear rivulet wavelength and thus strongly suggests that the departure of the wavelengths from the linear predictions is a true signature of wave dynamics along rivulets when transverse modulations are present.

We have already suggested that the transverse modulations of the waves are triggered by a Rayleigh-type instability mechanism much like with 2D pulses on planar substrates. We may check this possibility in view of the dependence of the transition II$_{\rm w}$-II$_{\rm m}$ in a parameter space limited to Ma and Re, that is for given liquid properties and a set of control parameters reduced to the temperature difference $T_w - T_a$ and the flow rate. If a Rayleigh-type instability occurs, the instability should start at the point of greatest slope $\partial_x h$. In the 'drag-inertia' regime, the maximum gradient of the free surface is observed at the front of the main hump and corresponds to the balance of inertia $\propto (q/h)\delta\partial_x h$ and the pressure gradient induced by surface tension $\propto \partial_{xxx} h$. Since q and h are $O(1)$, $\delta\partial_x h \sim \partial_{xxx} h$ gives a typical dimensionless length scale for the x coordinate $\propto \delta^{-1/2}$ which implies a typical slope $\partial_x h \propto \delta^{1/2}$. Making the analogy with the Rayleigh instability of a plane liquid-gas interface upside down (i.e. the gas is below the liquid), inclined from the horizontal with a slope $\partial_x h$, surface tension $\propto \partial_{zz} h \propto \lambda_{\rm Ray}^{-1/2}$ should balance the destabilizing gravity component normal to free surface $\propto \partial_x h \propto \delta^{1/2}$ as discussed above. This defines a critical wavelength $\lambda_{\rm Ray} \propto \delta^{-1/4}$. As a consequence, the rivulets may develop a transverse instability when their spatial extension $\lambda_{\rm riv}$ approaches $\lambda_{\rm Ray}$. Since from (12), $\lambda_{\rm riv} \propto {\rm Re}^{1/18}{\rm Ma}^{-1/2}$ and $\lambda_{\rm Ray} \propto {\rm Re}^{-11/36}$, $\lambda_{\rm riv} \sim \lambda_{\rm ray}$ gives ${\rm Re} \sim {\rm Ma}^{18/13}$ at the transition II$_{\rm w}$-II$_{\rm m}$. This result should be taken with care since it relies on very simple geometrical arguments and on the asymptotic behavior of 2D solitary waves in the drag-inertia regime, i.e. $\delta \to \infty$ — while the transition II$_{\rm w}$-II$_{\rm m}$ rather occurs in the intermediate regime between drag-gravity and drag-inertia (see Fig. 6). In particular, the variation of the local Reynolds number due to the channeling effects in the regime II$_{\rm w}$ is not taken into effect. However, the above analysis does recover the right tendency of a transition II$_{\rm w}$-II$_{\rm m}$ that occurs for smaller wavelengths as both the Marangoni and/or the Reynolds numbers are increased.

Figure 12*a* depicts a snapshot of the evolution at $t = 1480$ for the isothermal case with Re = 8. Note that for this case $E_x \approx E_z \approx cst$ from $t = 500$ up to $t = 10000$ and hence the snapshot in the figure corresponds to a fully developed 3D wave regime. Fig. 12*b* shows a snapshot of the evolution at the same moment in time with the same Reynolds number but with a large value of the Marangoni number, Ma = 100. The figure reveals the continuous competition between rewetting, point A, and dewetting, point B, in the regime of groovelike structures. Eventually point B wins the competition and a dewetting line appears across the domain. Hence, unlike the regime of ridgelike structures where rupture is a 'homogeneous' process appearing to occur between each pair of rivulets (see e.g. Fig. 8*a*), the rupture observed here in the groovelike regime for Re = 8 is rather localized in space. The reason is that we are very close to the transition II-III (see Fig. 11); this also explains the coexistence of a groove leading to rupture on the left of Fig. 12*b* (typical of region II as for Fig. 12*c* for Re = 7) with a region without rivulet on the right (as for isothermal conditions in Fig. 12*a*).

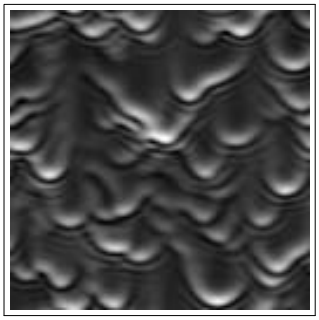

(a) $t = 1480$ - $\delta = 3.24$ - $\mathcal{M} = 0$ - {0.593,2.048}

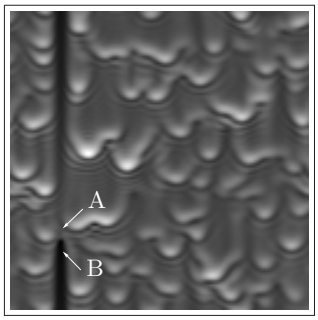

(b) $t = 1480$ - $\delta = 3.24$ - $\mathcal{M} = 1.62$ - {0.016,2.789}

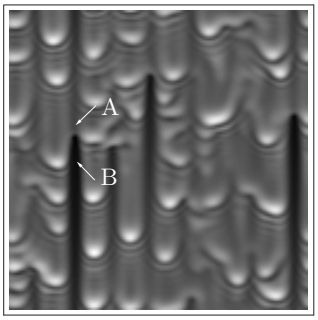

(c) $t = 1040$ - $\delta = 2.75$ - $\mathcal{M} = 1.72$ - {0.055,2.504}

FIG. 12: Wave patterns: (a) Re = 8, Ma = 0; (b) Re = 8, Ma = 100; (c) Re = 7, Ma = 100; with $\Gamma = 3375$, Bi = 0.1 and Pr = 7. Extrema are given in brackets. 'A' denotes a dewetting front and 'B' a rewetting one.

IX. HEAT TRANSFER ENHANCEMENT

Of particular practical interest for flows in the presence of rivulet structures is the evaluation of a possible enhancement of heat transfer. For this purpose we define an *overall heat transfer coefficient*, noted U, and based on the difference between the two extreme temperatures, $T_{\rm w}$ and $T_{\rm a}$, in the system. The corresponding overall heat transfered then simply reads:

$$Q = A_{\rm w} U (T_{\rm w} - T_{\rm a}) \,, \tag{13}$$

where $A_{\rm w}$ is the heated wall area. To estimate U in (13), we calculate the instantaneous amount of heat Q transfered from the free surface to the atmosphere, on the basis of:

$$Q = A_{\rm s} \alpha_g (\langle T_{\rm s} \rangle - T_{\rm a}) \,, \tag{14}$$

where $A_{\rm s}$ is the interfacial area and $\langle T_{\rm s} \rangle$ is the averaged interfacial temperature over the computational domain. Eliminating Q from (13) and (14) yields

$$U = \alpha_g \frac{A_{\rm s}}{A_{\rm w}} \frac{\langle T_{\rm s} \rangle - T_{\rm a}}{T_{\rm w} - T_{\rm a}}. \tag{15}$$

Since α_g, $A_{\rm w}$, $T_{\rm w}$ and $T_{\rm a}$ are constant, U can only be influenced by $A_{\rm s}$ and $\langle T_{\rm s} \rangle$. Note that for the Nusselt flat film solution, $U_{\rm N} = \alpha_g \theta_{\rm N} = \alpha_g / (1 + {\rm B})$. Therefore, the heat transfer enhancement, denoted HTE, for a wavy interface as compared to a flat interface can be defined as :

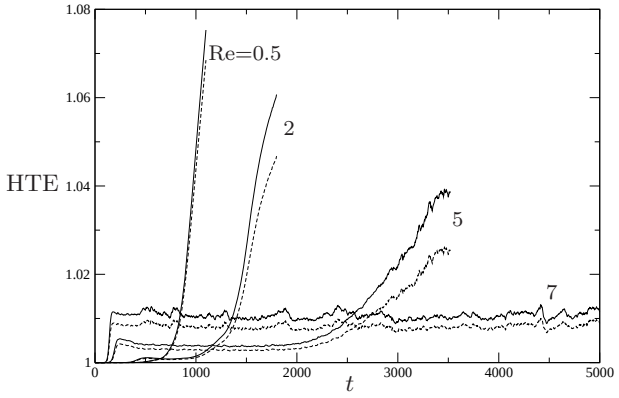

FIG. 13: Heat transfer enhancement (solid lines) for different Reynolds numbers and with Ma = 50; Dashed lines show the contribution to HTE only due to surface deformations $A_{\rm s}^*$.

$$\text{HTE} \equiv \frac{U}{U_{\rm N}} = A_{\rm s}^* \, \langle \theta \rangle \, (1 + B) \,, \tag{16}$$

where $A_{\rm s}^*$ is the ratio between the actual (instantaneous) free surface area and its value in the Nusselt state. The values HTE calculated for the structures in Figs. 5 are 1.06 (*a*), 1.04 (*b*), 1.007 (*c*) and 1.035 (*d*). While 3D solitary waves are indeed known to enhance heat transfer compared to regular waves [2] —*i.e.* 3.5% for Fig. 5*d* instead of 0.7% for Fig. 5*c*—, rivulet structures enable to reach the same enhancement or even better for much smaller flow rates, even though only in the vicinity of rupture. Indeed, HTE grows until rupture as shown in Fig. 13 (solid lines) and the time at which heat transfer starts to be significantly enhanced by rivulets is quite short. This demonstrates that heat transfer can be enhanced at much smaller flow rates than in the fully developed 3D wave regime (region III in the regime map in Fig. 11). What is therefore needed is to enlarge the time duration at which this happens, which is actually feasible provided the following:

(i) Rivulet structures should be triggered at the inlet through external perturbations with a wavelength given by (12) (due to the fact that the linear prediction in (12) fits well the nonlinear regime). Otherwise one would have to wait for a long distance down the channel for the heat transfer coefficient to increase (e.g. for Re = 5, the heat transfer coefficient starts to increase after ~ 2000 time units, i.e. approximatively 2m from the inlet).

(ii) The wall should be perfectly wetted by the liquid such that the thin regions between rivulets are stabilized by intermolecular forces and no rupture occurs.

Provided now that the computational domain in the streamwise direction, L_x, is sufficiently long, the evolution obtained from our simulations should then be qual-

itatively similar to the spatial evolution in experiments with long test sections. The result should thus be a large heat transfer throughout the whole domain at relatively small flow rate.

Finally, it is worth mentioning that it is the increase of the interfacial area A_s^* that mainly contributes to HTE while the surface temperature only plays a secondary role. This especially holds for rivulet regimes.

X. CONCLUSIONS

We have studied the 3D dynamics of a heated film flowing down a vertical wall. This has been achieved by first developing a system of four coupled equations for the evolution in space and time of the film thickness h, the interfacial temperature θ and the streamwise and spanwise flow rates, q and p respectively, given by (6), that allows a full description of the competition between hydrodynamic waves and thermocapillary Marangoni effect. The presence of rivulets aligned with the flow and large amplitude waves at their crests has been found in a region corresponding to the transition between drag-gravity and drag-inertia regimes. The boundaries of this (intermediate) region have been accurately determined and found to be shifted toward larger Reynolds numbers for increasing Marangoni number (as shown in the regime map of Fig. 11).

The competition between two distinct mechanisms is responsible for the change of behavior observed between drag-gravity and drag-inertia regime, *i.e.* in region II, corresponding precisely to the occurrence of waves riding the rivulets. The first mechanism is stabilizing due to surface tension: it tends to decrease the amplitude of hydrodynamic waves due to the presence of a streamwise pressure gradient between humps (where the spanwise curvature is larger) and flat zones (where the spanwise curvature is smaller). The second mechanism is destabilizing due to inertia: it tends to increase the amplitude of hydrodynamic waves due to the local increase of the flow rate (i.e. the local Reynolds number) in the rivulets. The fact that region II is characterized by stable quasi-2D solitary-like waves makes it attractive for the study of such waves experimentally. Further, both rivulets and solitary-like waves are known to improve heat and mass transfer in industrial processes, while film rupture is non desirable as it may lead to dry patch formation followed by overheating and damage of the solid substrate. However, only stabilizing long-range van der Waals intermolecular interactions can prevent film rupture and stabilize the thinning of the residual film. Moreover, the subcritical nature of the primary bifurcation for the thermocapillary instability [35] does not allow the construction of stationary transverse solutions corresponding to rivulets unless of course van der Waals forces are included in the model. This and related issues will be addressed in a future study.

Acknowledgments

The authors thank Paul Manneville, Manuel Velarde and Oleg Kabov for fruitful discussions. BS and CRQ thank both French and Belgium research agencies (CNRS/CGRI-FNRS) for having facilitated this research through the Tournesol project. SK acknowledges financial support from the EPSRC through an Advanced Fellowship. BS and PC thank the French Community of Belgium for their support through the ARCHIMEDES project (ARC 04/09-308). BS acknowledges financial support from the PRODEX program managed by the European Space Agency and by the Belgian Federal Science Policy Office, while PC acknowledges financial support of the 'Fonds de la Recherche Scientifique – F.N.R.S'.

APPENDIX A: WEIGHTED RESIDUAL METHOD AND REGULARIZATION

We give in this appendix the details of the procedure that allow us to reduce the basic system of equations (2) and boundary conditions (4) to the model (6) used in the rest of the paper. As mentioned in the text, it is based on the weighted residuals procedures applied for the 2D heated case [23] and the 3D isothermal case [10], and in which the velocity components in the x and z directions and the temperature field were expanded on polynomials (polynomials were chosen because they form a complete basis and a closed set with respect to the diferentiations and products involved in the governing equations). Truncation of the system of equations to be solved at $O(\epsilon)$ shows that the velocity and temperature fields can be represented at that order by a limited set of polynomials of the natural similarity variable $\bar{y} = y/h$ (the boundary conditions in terms of $\bar{y}$ are applied at $\bar{y} = 0$ and $\bar{y} = 1$). Velocity and temperature field were thus expanded as

$$\begin{aligned} u &= \frac{3}{h}\left(q - s_1 - s_2 - s_3\right) F_0(\bar{y}) + 45\frac{s_1}{h}F_1(\bar{y}) \\ &\quad + 210\frac{s_2}{h}F_2(\bar{y}) + 434\frac{s_3}{h}F_3(\bar{y}), \qquad \text{(A1a)} \\ w &= \frac{3}{h}\left(p - r_1 - r_2 - r_3\right) F_0(\bar{y}) + 45\frac{r_1}{h}F_1(\bar{y}) \\ &\quad + 210\frac{r_2}{h}F_2(\bar{y}) + 434\frac{r_3}{h}F_3(\bar{y}), \qquad \text{(A1b)} \\ T &= 1 + \left(\theta - 1 - t_1 - t_2 - t_3\right) G_0(\bar{y}) - \frac{3}{2}t_1 G_1(\bar{y}) \\ &\quad + \frac{5}{2}t_2 G_2(\bar{y}) - \frac{15}{4}t_3 G_3(\bar{y}), \qquad \text{(A1c)} \end{aligned}$$

where the polynomials F_i and G_i are defined below

$$\begin{aligned} F_0 &= \bar{y} - \frac{1}{2}\bar{y}^2 \\ F_1 &= \bar{y} - \frac{17}{6}\bar{y}^2 + \frac{7}{3}\bar{y}^3 - \frac{7}{12}\bar{y}^4 \\ F_2 &= \bar{y} - \frac{13}{2}\bar{y}^2 + \frac{57}{4}\bar{y}^3 - \frac{111}{8}\bar{y}^4 + \frac{99}{16}\bar{y}^5 - \frac{33}{32}\bar{y}^6 \end{aligned}$$

$$
\begin{aligned}
F_3 &= \bar{y} - \frac{531}{62}\bar{y}^2 + \frac{2871}{124}\bar{y}^3 - \frac{6369}{248}\bar{y}^4 + \frac{29601}{2480}\bar{y}^5 \\
&\quad - \frac{9867}{4960}\bar{y}^6 , \\
G_0 &= \bar{y} \\
G_1 &= \bar{y} - \frac{5}{3}\bar{y}^3 \\
G_2 &= \bar{y} - 7\bar{y}^3 + \frac{32}{5}\bar{y}^4 \\
G_3 &= \bar{y} - \frac{56}{3}\bar{y}^3 + \frac{192}{5}\bar{y}^4 - 21\bar{y}^5 .
\end{aligned}
$$

This set of polynomial test functions has been constructed to satisfy the orthogonality condition $\int_0^1 F_i\, F_j d\bar{y} \propto \delta_{ij}$ and $\int_0^1 G_i\, G_j d\bar{y} \propto \delta_{ij}$ with the help of a Gram-Schmidt orthogonalization procedure as well as to satisfy the Dirichlet boundary conditions at the solid wall. Representation (A1) contains a sufficient number of variables (q,p, s_i and r_i) to approximate u and T at order ϵ (the error being $O(\epsilon^2)$). Details and justifications can be found in [23]. Note that the functions F_1 and F_2 have been chosen so that they correspond exactly to the polynomials introduced in the isothermal case [8]. The introduction of the polynomial F_3 is made necessary by the Marangoni effect which modifies the stress conditions at the interface (4c-4d).

In projections (A1), twelve independent 2D fields are introduced to describe the 3D dynamics of heated falling films: the streamwise and spanwise flow rates $q = \int_0^h u\,\mathrm{d}y$ and $p = \int_0^h w\,\mathrm{d}y$, respectively, the interfacial temperature θ, the six correction fields s_i and r_i ($i = 1, 2, 3$) corresponding to the polynomial test functions F_i and accounting for the deviations of the velocity profiles away from the zeroth-order parabolic profile F_0, and the three correction fields t_i corresponding to the polynomial test functions G_i and accounting for the deviations of the temperature profile from the zeroth-order linear profile G_0. These polynomial expansions are then substituted into the governing equations which are then projected on the test functions according to the Galerkin method, yielding the residuals $\mathcal{R}_{i,q} = \langle E_q, F_i\rangle$, $\mathcal{R}_{i,p} = \langle E_p, F_i\rangle$ and $\mathcal{R}_{i,\theta} = \langle E_\theta, G_i\rangle$ where the inner product for any two functions f and g is defined as $\langle f, g\rangle = \int_0^h f\, g\,\mathrm{d}y$, and E_q, E_p and E_θ represent the boundary-layer equations (2a-2b) and the energy equation (2d), respectively. Since the boundary conditions at the interface (4c–4e) are non-homogeneous, they cannot be satisfied from the start by the test functions F_i, G_i. Instead these boundary conditions must be satisfied by the approximate solution itself and become therefore a new constraint on the amplitudes s_i, r_i, t_i, like in a tau-method (see [46] for details).

The evaluation of the residuals $\mathcal{R}$ yield a system of twelve evolution equations for the thirteen unknowns, h, q, p, θ, s_i r_i and t_i, with $i = 1, 2, 3$, to be completed by the mass balance equation obtained through integration of the kinematic boundary condition (2c) across the layer depth using the wall boundary conditions (4a) and the kinematic boundary condition (4b):

$$\partial_t h + \partial_x q + \partial_z p = 0\,.$$

This system forms the *full second-order model* whose treatment is feasible but cumbersome and laborious.

Here, we shall instead simplify the full second-order model following the procedure applied by Scheid *et al.* [10] for isothermal films. These authors attempted to simplify the full second-order isothermal model via slaving the correction fields s_i and r_i to h and q (and their derivatives) – effectively, by performing gradient expansions for these corrections. However, the elimination of these corrections resulted in second-order inertia terms which are highly nonlinear and as a consequence led to unrealistic behavior of the bifurcation diagrams for single-hump (2D) solitary waves ('primary homoclinic orbits' of the associated dynamical system) for the speed of the waves as a function of Reynolds number consisting of turning points and branch multiplicity (unlike the full second-order model which predicts the continuing existence of solitary wave solutions and is in agreement with full Navier-Stokes). A similar behavior is also observed with the Benney-like long-wave evolution equation, it is responsible for finite-time blow-up (as first observed by Pumir *et al.* [47]) and it is ultimately connected with the high-order inertia nonlinearities. So even for isothermal conditions, the reduced second-order model obtained from the full second-order one by eliminating s_i and r_i suffers from the same limitations (instead, the full second-order model is robust and without any blow-up behavior).

Scheid *et al.* [10] then cured the deficiencies of the reduced model by employing a Padé-like systematic regularization procedure to obtain a model consistent up to $O(\varepsilon^2)$ (an early version of this procedure is given in [23] for 2D heated films) which avoids finite-time blow-up due to high-order nonlinearities when increasing the Reynolds number. However, this regularization procedure here is only applied to the residuals corresponding to the boundary-layer equations, and not to the energy equation (for details the reader is referred to [23]). This assumption remains consistent with the gradient expansion at second order [48] since the interfacial temperature θ is coupled to the local flow rates q and p through its gradient, already of $O(\varepsilon)$. Therefore, the evolution equation for θ is directly obtained from the first residual $\langle E_\theta, G_0\rangle$ with $t_1 = t_2 = t_3 = 0$. Now, the first-order expressions of the fields s_1, s_2, s_3, r_1, r_2 and r_3 are obtained from the truncation at $O(\varepsilon)$ of the residuals corresponding to the test functions F_1, F_2 and F_3:

$$
\begin{aligned}
s_1 &= \delta\left[\frac{1}{210}h^2\partial_t q + \frac{19}{1925}\left(hp\partial_z q - pq\partial_z h - q^2\partial_x h\right)\right. \\
&\quad \left. + \frac{74}{5775}hq\partial_x q + \frac{17}{5775}hq\partial_z p\right] + \frac{1}{40}\mathcal{M}\,h^2\partial_x\theta\,, \\
s_2 &= \delta\left[-\frac{2}{5775}\left(hp\partial_z q - pq\partial_z h - q^2\partial_x h\right)\right.
\end{aligned}
$$

$$-\frac{2}{17325}hq\partial_x q+\frac{4}{17325}q\partial_z p\Big]-\frac{299}{53760}\mathcal{M}\,h^2\partial_x\theta\,,$$

$$s_3 \;=\; \frac{5}{3584}\mathcal{M}\,h^2\partial_x\theta\,,$$

$$r_1 \;=\; \delta\left[\frac{1}{210}h^2\partial_t p+\frac{19}{1925}\left(hq\partial_x p-qp\partial_x h-p^2\partial_z h\right)\right.$$
$$\left.+\frac{74}{5775}hp\partial_z p+\frac{17}{5775}hp\partial_x q\right]+\frac{1}{40}\mathcal{M}\,h^2\partial_z\theta\,,$$

$$r_2 \;=\; \delta\left[-\frac{2}{5775}\left(hq\partial_x p-qp\partial_x h-p^2\partial_z h\right)\right.$$
$$\left.-\frac{2}{17325}hp\partial_z p+\frac{4}{17325}p\partial_x q\right]-\frac{299}{53760}\mathcal{M}\,h^2\partial_z\theta\,,$$

$$r_3 \;=\; \frac{5}{3584}\mathcal{M}\,h^2\partial_z\theta\,,$$

Substituting these expressions in the first residuals $\mathcal{R}_{0,q}=\langle E_q,g_0\rangle$ and $\mathcal{R}_{0,p}=\langle E_p,g_0\rangle$, produces second-order inertia terms ($\propto\delta^2$), formally written as $\mathcal{R}^{(2),\delta}_{0,q}$ and $\mathcal{R}^{(2),\delta}_{0,p}$. These terms contain high-order nonlinearities that we next eliminate by appropriately adjusting algebraic prefactors or 'preconditioners'. Hence, we look for residuals $\mathcal{R}_{0,q}$ and $\mathcal{R}_{0,p}$ in the form $\mathcal{G}_q^{-1}\mathcal{F}_q$ and $\mathcal{G}_p^{-1}\mathcal{F}_p$ where $\mathcal{F}_q$ and $\mathcal{F}_p$ correspond to the expressions of the residuals $\mathcal{R}_{0,q}$ and $\mathcal{R}_{0,p}$ when a parabolic velocity profile is assumed, i.e. when corrections s_i and r_i are neglected. Isolating inertia terms, we thus set $\mathcal{G}_q\left(\mathcal{R}^{(1),\delta}_{0,q}+\mathcal{R}^{(2),\delta}_{0,q}\right)=\mathcal{R}^{(1),\delta}_{0,q}$ and $\mathcal{G}_p\left(\mathcal{R}^{(1),\delta}_{0,p}+\mathcal{R}^{(2),\delta}_{0,p}\right)=\mathcal{R}^{(1),\delta}_{0,p}$, where superscripts 1 and 2 refer to first- and second-order inertia terms. The zeroth-order expressions of the flow rates $q=h^3/3+O(\varepsilon)$ and $p=O(\varepsilon)$ are next invoked to reduce the degree of nonlinearities of the regularization factors $\mathcal{G}_q$ and $\mathcal{G}_p$. Consequently, the inertia terms $\mathcal{R}^{(2),\delta}_{0,q}$ and $\mathcal{R}^{(2),\delta}_{0,p}$ induced by deviations of the streamwise and spanwise velocity components from the parabolic profile appear asymptotically at $O(\varepsilon^2)$ and $O(\varepsilon^3)$, respectively. We therefore obtain $\mathcal{G}_q\equiv\left[1-\frac{\delta}{70}q\partial_x h+\mathcal{M}\left(\frac{5}{56}\frac{\partial_x\theta}{h}+\frac{1}{224}\frac{\partial_{xx}\theta}{\partial_x h}\right)\right]^{-1}$ and $\mathcal{G}_p=1$. Though h cannot be exactly zero ($h=0$ at rupture, but here we only consider the dynamics prior to rupture), $\partial_x h$ does vanish at certain points in the domain. The last term in $\mathcal{G}_q$ will thus lead to a singularity if kept in its present form and should be taken out from the inertia terms $\mathcal{R}^{(2),\delta}_{0,q}$ (the singularity arises because of the different order of differentiation for h and θ in the quotient $\partial_{xx}\theta/\partial_x h$). As much as *ad-hoc* this step might appear, it is necessary if we want a relatively simple model without mixed time/space derivatives; indeed, one can formally cure the singularity by changing the algebraic preconditioner to a differential operator, following the example of Ooshida [36]. The regularized model is finally obtained and given in (6).

[1] P. Manneville, *Dissipative Structures and Weak Turbulence* (Academic Press, New York, 1990).

[2] S. V. Alekseenko, V. E. Nakoryakov, and B. G. Pokusaev, *Wave flow in liquid films* (Begell House (New York), 1994), 3rd ed.

[3] J. Liu, J. B. Schneider, and J. P. Gollub, Phys. Fluids **7**, 55 (1995).

[4] C. D. Park and T. Nosoko, AIChE J. **49**, 2715 (2003).

[5] P. L. Kapitza and S. P. Kapitza, in *Collected papers of P. L. Kapitza (1965)*, edited by D. T. Haar (Pergamon (Oxford), 1949), pp. 690–709, (Original paper in Russian: Zh. Ekper. Teor. Fiz. **19**, 105–120).

[6] V. Ya. Shkadov, Izv. Ak. Nauk SSSR, Mekh. Zhidk Gaza, Mekh. Zhi. Gaza **1**, 63 (1977).

[7] E. A. Demekhin and V. Ya. Shkadov, Izv. Ak. Nauk SSSR, Mekh. Zhidk Gaza, Mekh. Zhi. Gaza **5**, 21 (1984).

[8] C. Ruyer-Quil and P. Manneville, Eur. Phys. J. B **15**, 357 (2000).

[9] C. Ruyer-Quil and P. Manneville, Phys. Fluids **14**, 170 (2002).

[10] B. Scheid, C. Ruyer-Quil, and P. Manneville, J. Fluid Mech. **562**, 183 (2006).

[11] V. Ludviksson and E. N. Lightfoot, AIChE J. **14**, 620 (1968).

[12] R. B. Bird, W. E. Stewart, and E. N. Lightfoot, *Transport Phenomena* (John Wiley & Sons (New York), 1960).

[13] O. A. Kabov, E. A. Chinnov, and J. C. Legros, In Proceedings of the Conference on Transport Phenomena with Moving Boundaries, $11^{th}-12^{th}$ October, Berlin, Germany (2003).

[14] E. A. Chinnov and O. Kabov, Journal of Applied Mechanics and Technical Physics **44**, 708 (2003).

[15] E. A. Chinnov and O. Kabov, High Temperature **42**, 269 (2004), translated from Teplofizika Vysokikh Temperatur.

[16] D. V. Zaitsev and O. A. Kabov, Experiments in Fluids **39**, 712 (2005).

[17] B. D. D. Holland and S. Wilson, J. Fluid Mech. **441**, 195 (2001).

[18] D. A. Goussis and R. E. Kelly, J. Fluid Mech. **223**, 25 (1991).

[19] K. A. Smith, J. Fluid Mech. **24**, 401 (1966).

[20] S. W. Joo, S. H. Davis, and S. G. Bankoff, J. Fluid Mech. **321**, 279 (1996).

[21] B. Scheid, C. Ruyer-Quil, U. Thiele, O. A. Kabov, J. C. Legros, and P. Colinet, J. Fluid Mech. **527**, 303 (2005).

[22] B. Ramaswamy, S. Krishnamoorthy, and S. W. Joo, J. Comp. Phys. **131**, 70 (1997).

[23] C. Ruyer-Quil, B. Scheid, S. Kalliadasis, M. G. Velarde, and R. Kh. Zeytounian, J. Fluid Mech. **538**, 199 (2005).

[24] C. Ruyer-Quil and P. Manneville, Eur. Phys. J. B **6**, 277 (1998).

[25] J. P. Burelbach, S. G. Bankoff, and S. H. Davis, J. Fluid Mech. **195**, 463 (1988).

[26] S. W. Joo and S. H. Davis, Phys. Fluids **3**, 231 (1991).

[27] A. Oron, S. H. Davis, and S. G. Bankoff, Rev. Mod. Phys.

69, 931 (1997).
[28] W. H. Press, S. A. Teukolsky, W. T. Vetterling, and B. P. Flannery, *Numerical recipes in C - The Art of Scientific Computing* (Cambridge University Press (New York), 1992), 2nd ed.
[29] M. Bestehorn, A. Pototsky, and U. Thiele, Eur. Phys. J. B **33**, 457 (2003).
[30] S. Saprykin, P. Trevelyan, R. Koopmans, and S. Kalliadasis, Phys. Rev. E **75**, 026306 (2007).
[31] B. Scheid, C. Ruyer-Quil, S. Kalliadasis, M. G. Velarde, and R. Zeytounian, J. Fluid Mech. **538**, 223 (2005).
[32] P. M. J. Trevelyan, B. Scheid, C. Ruyer-Quil, and S. Kalliadasis, J. Fluid Mech. **592**, 295 (2007).
[33] A. Oron, Phys. Fluids **12**, 1633 (2000).
[34] W. Boos and A. Thess, Phys. Fluids **11**, 1633 (1999).
[35] S. J. VanHook, M. F. Schatz, J. B. Swift, W. D. McCormick, and H. L. Swinney, J. Fluid Mech. **345**, 45 (1997).
[36] T. Ooshida, Phys. Fluids **11**, 3247 (1999).
[37] S. Kalliadasis and H.-C. Chang, J. Fluid Mech. **261**, 135 (1994).
[38] C. Duprat, C. Ruyer-Quil, S. Kalliadasis, and F. Giorgiutti-Dauphiné, Phys. Rev. Lett. **98**, 244502 (2007).
[39] E. N. Kalaidin, S. Y. Vlaskin, E. A. Demekhin, and S. Kalliadasis, Dokl. Phys. **50**, 668 (2005).
[40] E. A. Demekhin, E. N. Kalaidin, S. Kalliadasis, and S. Y. Vlaskin, Phys. Fluids **19**, 114103 (2007).
[41] S. Saprykin, E. A. Demekhin, and S. Kalliadasis, Phys. Fluids **17**, 117105 (2005).
[42] S. V. Alekseenko, D. M. Markovich, and S. I. Shtork, Phys. Fluids **8**, 3288 (1996).
[43] B. Scheid, A. Oron, P. Colinet, U. Thiele, and J. C. Legros, Phys. Fluids **14**, 4130 (2002), erratum: *Phys. Fluids* **15**, 583 (2003).
[44] J. M. Skotheim, U. Thiele, and B. Scheid, J. Fluid Mech. **475**, 1 (2003).
[45] S. Kalliadasis, E. A. Demekhin, C. Ruyer-Quil, and M. G. Velarde, J. Fluid Mech. **492**, 303 (2003).
[46] B. A. Finlayson, *The method of weighted residuals and variational principles, with application in fluid mechanics, heat and mass transfer* (Academic Press, 1972).
[47] A. Pumir, P. Manneville, and Y. Pomeau, J. Fluid Mech. **135**, 27 (1983).
[48] The term 'gradient expansion' here and in our previous studies on film flows refers to the particular way we do the long-wave expansion: (i) ε is introduced from $\varepsilon \sim \partial_t, \partial_x, \partial_z$, i.e. it acts as an 'ordering parameter' instead of defining it e.g. from $\bar{h}_{\rm N}/\ell$ with ℓ an *a-priori* unknown long-scale in the streamwise/spanwise directions; (ii) the long-wave expansion with respect to ε is then carried out as usual, i.e. it is a perturbation expansion of all pertinent variables in powers of ε.